

Finding Belief Geometries with Sparse Autoencoders

Matthew Levinson*
Independent Researcher
good.epic@gmail.com

Abstract

Understanding the geometric structure of internal representations is a central goal of mechanistic interpretability. Prior work has shown that transformers trained on sequences generated by hidden Markov models encode probabilistic belief states as simplex-shaped geometries in their residual stream, with vertices corresponding to latent generative states. Whether large language models trained on naturalistic text develop analogous geometric representations remains an open question.

We introduce a pipeline for discovering candidate simplex-structured subspaces in transformer representations, combining sparse autoencoders (SAEs), k -subspace clustering of SAE features, and simplex fitting using AANet. We validate the pipeline on a transformer trained on a multipartite hidden Markov model with known belief-state geometry. Applied to Gemma-2-9B, we identify 13 priority clusters exhibiting candidate simplex geometry ($K \geq 3$).

A key challenge is distinguishing genuine belief-state encoding from *tiling artifacts*: latents can span a simplex-shaped subspace without the mixture coordinates carrying predictive signal beyond any individual feature. We therefore adopt *barycentric prediction* as our primary discriminating test. Among the 13 priority clusters, 3 exhibit a highly significant advantage on near-vertex samples (Wilcoxon $p < 10^{-14}$) and 4 on simplex-interior samples. Together 5 distinct real clusters pass at least one split, while no null cluster passes either. One cluster, 768_596, additionally achieves the highest causal steering score in the dataset. This is the only case where passive prediction and active intervention converge. We present these findings as preliminary evidence that genuine belief-like geometry exists in Gemma-2-9B’s representation space, and identify the structured evaluation that would be required to confirm this interpretation.

1 Introduction

A growing body of work shows that transformer language models organize their activations into structured geometric objects that encode variables relevant to prediction (Elhage et al., 2022; Cunningham et al., 2023; Bricken et al., 2023; Gurnee & Tegmark, 2024). One natural form such structure could take is a simplex. If the model maintains a probability distribution over discrete latent states, the barycentric coordinates of a simplex provide a natural internal representation of that distribution. We refer to representations with this structure as *belief geometries*.

Prior work demonstrates this concretely in controlled settings. Transformers trained on sequences from hidden Markov models develop simplex-shaped geometries in their residual stream, with vertices corresponding to latent states and barycentric coordinates encoding the model’s belief distribution (Shai et al., 2024; Piotrowski et al., 2025). Geometric structure has also been identified in algorithmic tasks: addition encoded via trigonometric representations (Kantamneni & Tegmark, 2025), and character counts on curved manifolds (Gurnee

*This work was supported by a scholarship and computational resources from Simplex AI Safety. The author thanks Paul Riechers, Adam Shai, and Xavier Poncini for their support.

et al., 2026). Whether analogous structures arise for the abstract latent variables of natural language such as discourse mode, referential context, or syntactic role remains an open question.

We introduce a pipeline for discovering candidate belief geometries in large pretrained language models, combining SAE representations with k -subspace clustering and AANet simplex fitting, a neural implementation of archetypal analysis that recovers barycentric coordinates over extreme-point vertices (Section 4.2). A central challenge is distinguishing genuine belief-state encoding from *tiling artifacts*: a group of co-activating latents may span a simplex-shaped subspace simply by covering different regions of a shared contextual variable, without encoding a genuine mixture. Such tiling would produce apparent simplex geometry while the best individual latent already captures the full predictive signal. We therefore adopt the *barycentric predictive advantage* as our primary test: genuine mixture encoding implies that the full coordinate vector predicts next-token behavior better than any single feature.

We first validate the pipeline on a controlled toy model where ground-truth belief geometry is known. We then apply it to Gemma-2-9B, identifying 13 priority clusters as candidates for detailed evaluation. The barycentric predictive advantage test is our primary discriminator: 3 of 13 real clusters pass on near-vertex samples ($p < 10^{-14}$), 4 pass on simplex-interior samples, and no null cluster passes on either split. Cluster 768.596 is the one case where passive prediction and active causal intervention jointly support a belief-geometry interpretation. We present highlight results for two clusters with the strongest causal and predictive signals, respectively, and discuss what structured evaluation would be required to move from these preliminary findings to a confirmed account of belief-state encoding in naturalistic text.

2 Related Work

Sparse autoencoders applied to transformer residual streams recover large collections of sparse, interpretable feature directions (Cunningham et al., 2023; Bricken et al., 2023), providing a natural basis for studying higher-order geometric structure. Beyond individual features, structured geometric objects have been identified in transformer representations: curved manifolds encoding numeric variables in algorithmic settings (Gurnee et al., 2026; Kantamneni & Tegmark, 2025), and linear subspaces encoding more abstracted numeric concepts of physical and calendar distance (Gurnee & Tegmark, 2024). Simplex representations are of particular interest because they encode probability distributions over discrete latent states through barycentric coordinates. Transformers have also been shown to perform implicit Bayesian inference (Akyürek et al., 2023; von Oswald et al., 2023; Xie et al., 2022), which suggests belief geometries as a potential encoding strategy. Simplices are related geometrically and conceptually to archetypal analysis (Cutler & Breiman, 1994), a statistical technique that looks for extreme points in a dataset from which other examples can be represented as convex combinations. This makes it a good technique for finding potential simplex vertices.

Most directly relevant is work showing that transformers trained on HMM-generated sequences represent belief distributions geometrically as simplices in the residual stream (Shai et al., 2024; Piotrowski et al., 2025), where barycentric coordinates encode the model’s belief distribution over latent states. Our work extends this line by introducing a method for discovering analogous structures in large pretrained models without access to ground-truth latent states, and by introducing the barycentric predictive advantage test to distinguish genuine mixture encoding from tiling artifacts. A key difference from algorithmic settings is that naturalistic discourse variables lack ground-truth labels, making confirmation of the belief-state interpretation contingent on structured evaluation infrastructure that does not yet exist, a gap we discuss in Section 7.2.

3 Toy Model: Proof of Concept

We validate the pipeline on a controlled multipartite hidden Markov model with known ground-truth belief geometry (Appendix A). The model combines five independent genera-

tive components with a joint vocabulary of 432 tokens, creating an intentionally challenging regime where each token encodes contributions from all five sources simultaneously. Applied to a small transformer trained on this model, the pipeline recovers all five components with no supervision (mean $R^2 = 0.61$ on held-out data; Table 4 in Appendix A), correctly identifying the underlying simplex dimension for each component via the elbow criterion.

4 Real Model Pipeline: Gemma-2-9B

In contrast to prior work that analyzes models trained on synthetic tasks or real tasks with known latent variables, our approach searches for simplex-structured representations in a large pretrained language model without access to ground-truth latent states. We apply our belief-geometry discovery pipeline to Gemma-2-9B, using a publicly released GemmaScope JumpReLU SAE for the residual stream at layer 20 ($d_{\text{SAE}} = 16,384$ latents; Bloom et al. 2024). The pipeline consists of four stages: 1) SAE decoder directions are clustered to identify groups of features that may jointly encode a single contextual variable; 2) we fit AANet to each candidate group using FineWeb sequences (Penedo et al., 2024) to test for simplex structure and recover barycentric coordinates; 3) we prioritize clusters whose fitted geometry is most consistent with a k -simplex ($k \geq 3$); 4) we evaluate priority clusters using predictive, causal, and semantic validation tests.

4.1 k -Subspace Clustering

We cluster all column-normalized decoder directions in W_d using a method that combines k -subspace clustering (Wang et al., 2009) with column-pivoted QR initialization (Damle et al., 2019). k -Subspace clustering partitions vectors into groups that each span a low-dimensional subspace, generalizing k -means from cluster centroids to cluster subspaces. We seed the algorithm using column-pivoted QR decomposition of the decoder matrix, which greedily selects a maximally spread set of initial subspace directions and substantially improves convergence over random initialization. We cluster decoder directions rather than token activations directly because decoder geometry captures which latents write into similar residual-stream subspaces, providing a model-based notion of features that may jointly encode a common contextual variable.

We run the pipeline at two resolutions, $K \in \{512, 768\}$, and retain candidate clusters with estimated rank $k \geq 3$.

4.2 AANet Simplex Fitting

AANet (van Dijk et al., 2019; Venkat et al., 2024) is an autoencoder-based implementation of archetypal analysis. It learns to embed data into a simplex of K vertices at the bottleneck layer, from which we extract barycentric coordinates expressed as convex combinations of K archetypal extreme points. Unlike classical archetypal analysis, AANet learns a nonlinear encoder and decoder jointly with the positions of the archetypes, making it robust to the curved geometry expected in large model activations.

For each candidate cluster, we form the cluster’s partial contribution to the residual stream at each token position t where at least one cluster latent is active:

$$\mathbf{x}_t = \tilde{\mathbf{f}}_t \mathbf{W}_d, \tag{1}$$

where $\tilde{\mathbf{f}}_t$ is the SAE latent activation vector with all non-cluster entries set to zero. We fit AANets for $K \in \{2, 3, 4, 5, 6, 7\}$ and identify clusters with an elbow in the reconstruction loss curve. We do not search for cases with $K = 2$ vertices, as a 1-simplex is not distinct from a linear feature.

4.3 Priority Cluster Selection

After clustering and AANet fitting across both $N = 512$ and $N = 768$ runs, we select 13 *priority clusters* for detailed validation (Table 1). Eleven have an AANet elbow at $K = 3$; two have an elbow at $K = 4$. Cluster sizes range from 4 to 26 latents.

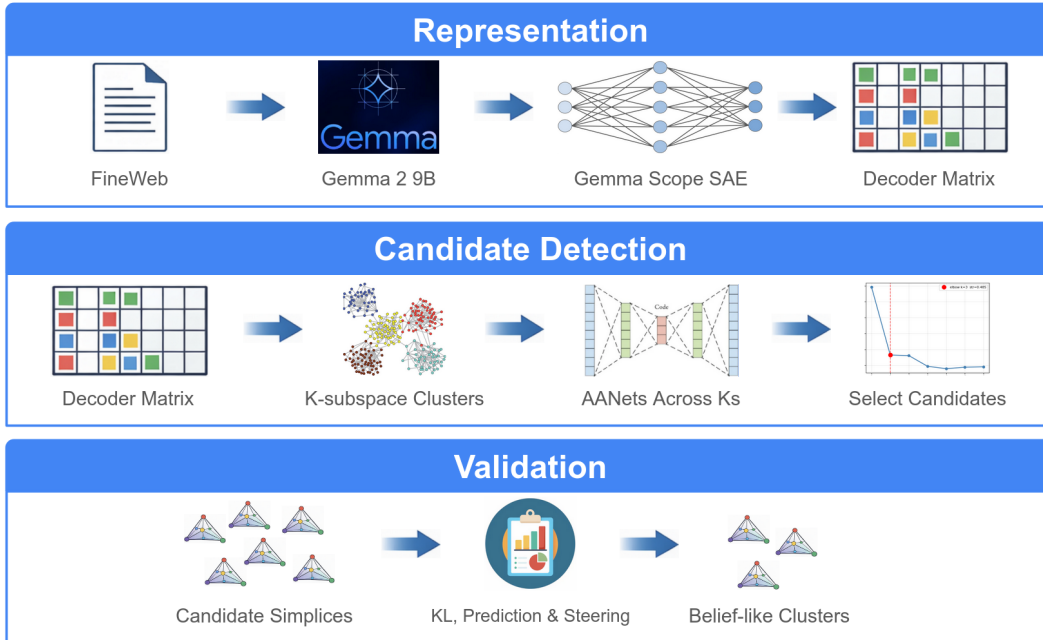


Figure 1: **Overview of the belief geometry discovery pipeline.** Text sequences are processed through Gemma-2-9B, and residual-stream activations at layer 20 are encoded by a GemmaScope JumpReLU SAE. Decoder directions of SAE latents are clustered into candidate latent groups using k -subspace clustering. Each candidate group is then fit with AANet to test for simplex structure and recover barycentric coordinates. The resulting candidate belief geometries are evaluated using barycentric predictive advantage and causal steering as the primary validation analyses.

For comparison, we construct *null clusters*. We partitioned the latents randomly into sets with the identical distribution of m as the true clusters. We retained the three that passed the same geometric screening criteria applied to real candidates, then ran the same validation pipeline. The goal was to test whether the pipeline over-selects spurious geometry. Note that even if we loosened the criteria, only three null clusters passed the first screen. The 13-to-3 asymmetry at the screening stage is itself consistent with real clusters exhibiting genuine low-dimensional structure.

5 Validation

We evaluate the 13 priority clusters and 3 null clusters using two main validation analyses. A central challenge is the *tiling artifact*. Groups of latents may span a subspace that can be projected onto a simplex because they cover different regions of a subspace leveraged by the model within a given context, without encoding a genuine mixture. In that case, the best individual latent already captures the full predictive signal, and the mixture coordinates add no value.

The barycentric predictive advantage is the primary discriminating test. It directly addresses the tiling artifact, and its result on the null clusters is the clearest single finding in the paper. Causal steering is the other main test. When predictable results from active intervention can be demonstrated, it is a stronger claim. In our case, we are searching for abstract latent mixtures with an analytical setup that yields wide confidence intervals. So our steering results are suggestive but not definitive. KL divergence and semantic coherence are supporting analyses.

Table 1: **The 13 priority clusters.** Clusters are identified by the number of clusters for the k -subspace clustering (512 or 768) and their cluster index. m denotes the number of SAE latents in the cluster. Vertex consistency is labeled as consistent, mixed, or inconsistent. Confidence is derived from 20-iteration autointerp synthesis: HIGH = ≥ 2 consistent vertices; MEDIUM = no inconsistent vertices; LOW = ≥ 1 inconsistent vertex.

Cluster	m	Semantic Confidence	Vertex interpretation (summary)
512.17	15	HIGH	Text register (instructional / promotional / metadata)
512.229	22	MEDIUM	Syntactic complexity (simple / formal-specific / complex-embedded)
512.261	18	MEDIUM	Grammatical function (content words / function words / technical register)
512.504	22	MEDIUM	Syntactic role (function words / content nouns / predicates)
768.140	26	MEDIUM	Referential specificity (generic / specific / anaphoric)
768.210	4	MEDIUM	Syntactic complexity (complex NP / simple / intermediate)
768.306	5	MEDIUM	Register formality (conversational / formal-technical / structured)
768.596	6	MEDIUM	Grammatical person / discourse role (3rd / 1st / 2nd person)
512.22	6	LOW	Grammatical role (nominal / function words / verbal)
512.67	25	LOW	Syntactic function (nominal-boundary / determiner-initiation / connective)
512.181	26	LOW	Syntactic role (content words / function words / specialized vocab)
512.471	10	LOW	Grammatical person / complexity (simple / third-formal / instructional)
768.581	11	LOW	Syntactic role (content words / function words / verbal predicates)

5.1 Barycentric Predictive Advantage

Setup. The primary test asks whether the full barycentric coordinate vector $\text{bary}_t \in \mathbb{R}^K$ predicts next-token behavior better than any single latent in the cluster. For each of the top-50 highest-variance tokens across near-vertex samples, we fit a linear model predicting the token’s log-probability from the barycentric coordinates (5-fold cross-validation, capped at 200 near-vertex samples per vertex). We separately fit the same prediction using each individual latent activation. Using a paired Wilcoxon signed-rank test, we compare the 50-vector of R^2_{bary} to the 50-vector of $R^2_{\text{best latent}}$, where the latent R^2 vector uses the highest R^2 across all individual latent models for each token.

Hypothesis. Genuine mixture encoding implies that the full barycentric representation should carry predictive signal not present in any single latent, directly ruling out the tiling artifact.

Results. Table 2 shows results for both evaluation splits. No null cluster exhibits a significant barycentric advantage on either. Among the 13 real clusters, 5 pass on near-vertex samples or interior samples, with two passing on both. This directly tests the defining prediction of the simplex hypothesis and rules out the tiling artifact for these clusters.

The simplex-interior split is the more informative test: near-vertex samples lie close to a single extreme, so a specialized latent can already do well; interior samples require the

Table 2: **Barycentric vs. best-latent predictive advantage, both evaluation splits.** *Frac. bary wins*: fraction of top-50 highest-variance tokens for which the barycentric coordinate achieves higher R^2 than the best individual latent. Wilcoxon p -values test the one-sided hypothesis that barycentric R^2 is stochastically greater. NV = near-vertex samples; SI = simplex-interior samples. No null cluster passes on NV. One null cluster passes SI; see text.

Cluster	n	Near-vertex (NV)		Simplex-interior (SI)	
		Frac. wins	p	Frac. wins	p
512.17	15	0.00	1.00	0.04	1.00
512.22	6	0.00	1.00	0.04	1.00
512.67	25	0.00	1.00	0.00	1.00
512.181	26	1.00	$< 10^{-15}$	1.00	$< 10^{-15}$
512.229	22	1.00	$< 10^{-15}$	0.58	0.003
512.261	18	0.00	1.00	0.16	1.00
512.471	10	0.00	1.00	0.84	5×10^{-9}
512.504	22	0.00	1.00	1.00	$< 10^{-15}$
768.140	26	0.20	1.00	0.04	1.00
768.210	4	0.00	1.00	0.00	1.00
768.306	5	0.16	1.00	0.00	1.00
768.581	11	0.00	1.00	0.00	1.00
768.596	6	0.98	$< 10^{-14}$	0.16	1.00
512.138 (null)	51	0.00	1.00	0.00	1.00
512.345 (null)	47	0.06	1.00	0.00	1.00
768.310 (null)	17	0.22	0.977	0.00	1.00

mixture coordinate to meaningfully shift token predictions, something no single latent can accomplish for a true mixture. Clusters 512.181 and 512.229 pass both splits ($p \approx 0$), providing the strongest evidence. Clusters 512.471 and 512.504 pass interior only; at the vertex extremes their near-vertex R^2 values are nearly identical for barycentric and best-latent predictions, consistent with a dominant latent at each extreme. Cluster 768.596 passes near-vertex only (interior: frac. wins = 0.16, mean R^2 : -0.003 vs. 0.093), indicating its advantage is specific to the vertex extremes. Together, 5 real clusters pass at least one split versus 0 null clusters on either, a signal we take as evidence that the pipeline is finding real structure.

Distributional sanity check. As a complementary check, we compute the ratio of cross-vertex to same-vertex symmetric KL divergence between next-token distributions at near-vertex positions. If vertex assignments are functionally meaningful, cross-vertex pairs should predict more divergent continuations. All 13 real clusters achieve ratios above 1 (1.017–1.987), confirming that vertex assignments correspond to genuinely different distributional regimes. However, null clusters also achieve ratios above 1 (1.108–1.329), so this check is not discriminating on its own; we treat it as a sanity check that the near-vertex samples are at distributional extremes, not as evidence for belief-geometry encoding. Full per-cluster values are in Appendix G.

5.2 Causal Steering

Semantic prerequisite. Interpreting a steering score requires first establishing that the vertex labels are meaningful. For each cluster, we run 20 independent labeling rounds with Claude Sonnet 4.5 and measure *document accuracy* via Qwen-2.5-72B-AWQ classifying held-out near-vertex continuations against the synthesized vertex labels (details in Appendix E). We require a mean score ≥ 0.15 on at least 2 of K vertices before a cluster *qualifies* for steering evaluation. Five real clusters do not qualify; all three null clusters contain at least one vertex below this threshold, though semantic coherence is not otherwise discriminating. Consolidated interpretations are in Table 1 and Appendix G.

Table 3: **Causal steering scores.** Null cluster scores overlap with those of most qualifying real clusters; 768_596 is the only cluster where a significant barycentric advantage and a positive steering score converge.

Cluster	Steering score	Best type	Best scale
768_596	0.419	type2	20
512_22	0.356	type1	20
768_210	0.336	type2	1
768_140	0.289	type1	20
512_67	0.250	type1	20
512_261	0.242	type1	1
768_581	0.209	type3	5
512_17	0.118	type3	5
512_138 (null)	0.358	type1	1
768_310 (null)	0.272	type1	20
512_345 (null)	0.150	type1	5

Setup. For qualifying clusters, we test whether the simplex geometry is causally relevant by steering the model’s residual stream toward target vertex coordinates. For each source vertex v and target $v' \neq v$, we compute an intervention direction from the AANet vertex decoder, add it at scale $s \in \{1, 5, 20\}$, and generate a continuation. We evaluate each continuation using Qwen-2.5-72B (AWQ quantized, via vLLM), which classifies whether the continuation matches the target vertex’s semantic description. The steering score is the mean classification accuracy across source-target pairs, intervention types (Appendix E), and scales.

Results. All 8 qualifying real clusters achieve positive steering scores (Table 3). However, null cluster scores (0.150–0.358) overlap substantially with those of most qualifying real clusters, limiting the discrimination this strand provides in aggregate. The most informative result is 768_596 (0.419), the only cluster where a significant barycentric predictive advantage and a positive steering score converge. Their joint occurrence in a single cluster is the strongest functional evidence we find. For the remaining qualifying real clusters, we do not treat steering scores as confirmatory evidence on their own.

6 Highlight Results

6.1 Cluster 768_596: Convergence of Prediction and Causal Intervention

Cluster 768_596 ($m = 6$ latents) has six latent centroids that partition into three vertex-preferring groups (Figure 2). The semantic interpretation points toward grammatical person as the organizing dimension: V0 corresponds to third-person or external-entity reference, V1 to first-person or self-referential framing, and V2 to second-person address and directive language. Each vertex is primarily supported by one or two dominant latents (Appendix H).

Two qualifications are important for interpreting the results. First, V2 is a *phantom vertex*: its document accuracy is 0.069, meaning the evaluator cannot reliably identify V2-typical content even in unsteered samples. The majority of near-vertex examples (8,258 of 10,536) land near V2, consistent with V2 representing a high-frequency default state rather than a semantically crisp pole. The real causal signal is in the V0 \leftrightarrow V1 directions (steering accuracy 0.667 and 0.429 respectively). Second, the barycentric predictive advantage holds on near-vertex samples but does not generalize to simplex-interior positions (interior: frac. bary wins = 0.16, mean R^2 : -0.003 vs. 0.093 for the best latent), suggesting the mixture encoding is concentrated near the vertex extremes.

With those caveats, 768_596 is nevertheless the only cluster where passive prediction and causal steering converge. Both signals are on the V0 \leftrightarrow V1 axis, which represents the seman-

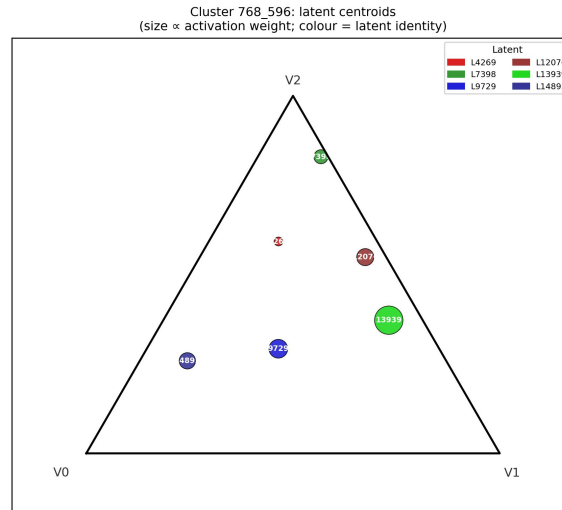


Figure 2: **Cluster 768_596: per-latent centroid positions.** Mean barycentric centroid of each of the six latents. The latents partition across the three vertices, consistent with vertex-specialized feature coding.

tically crisp part of the geometry. The near-vertex barycentric advantage ($p < 10^{-14}$) shows that V0 and V1 together encode information that neither latent captures alone. The steering score of 0.419 confirms that intervening on this axis shifts model behavior in the expected direction.

6.2 Cluster 512_181: Strongest Predictive Signal Across Both Sample Regimes

Cluster 512.181 ($m = 26$ latents) achieves the most unambiguous barycentric predictive advantage in the dataset, replicating across both evaluation splits: frac. bary wins = 1.00 on near-vertex samples ($p < 10^{-15}$, mean R^2 : 0.612 vs. 0.539) and 1.00 on simplex-interior samples ($p \approx 0$). The replication across near-vertex and interior regimes is distinctive: whereas 768_596’s advantage is specific to the vertex extremes, 512_181’s barycentric coordinates carry predictive signal across the full range of simplex positions.

This cluster does not qualify for causal steering evaluation (at least one vertex has document accuracy < 0.15), and its semantic confidence is rated LOW. The co-existence of a strong, replicating predictive signal with weak semantic interpretability raises two competing interpretations. One is that the barycentric coordinates encode a functional variable that is real but manifests through distributional statistics rather than lexical content, making it difficult to label from short continuations. Another is that the 26-latent cluster captures multiple overlapping contextual distinctions rather than a single simplex mixture, producing a strong predictive signal through aggregation rather than genuine belief-state encoding. The structured evaluation we outline in Section 7.2 would be needed to distinguish these.

7 Discussion

7.1 What the Barycentric Test Tells Us

The 5-versus-0 real-versus-null outcome is the central result. Priority clusters were selected on geometric grounds before any functional validation, so the contrast is not attributable to selection bias. For the five passing clusters, the simplex geometry encodes mixture information no single feature captures, directly ruling out the tiling artifact.

The four clusters passing interior only (512_471, 512_504) and the one passing near-vertex only (768_596) differ in *where* the mixture signal lives, not whether it exists. Clusters

failing entirely, including 768_140 (strongest KL signal, ratio 1.987), likely encode discrete distinctions already well-captured by a dominant individual latent. The barycentric test is the filter that separates candidates worth deeper investigation from those that are not.

7.2 Toward Structured Validation of Belief Geometries

The findings establish that the pipeline finds real structure and that the barycentric test discriminates real candidates from null. They do not, however, confirm the belief-state interpretation that simplex coordinates encode a genuine probability distribution over discrete latent states the model tracks as a hidden variable.

Prior work on geometric representations relied on structured, verifiable problems where the latent variable’s value is known, allowing representations to be probed against ground truth. Natural language discourse structure lacks these properties: labels like “grammatical person” or “referential specificity” are not discretely verifiable from a single token. This paper is a first attempt to extend the search to this more abstract setting, and the gap it exposes is precisely the absence of the structured, verifiable datasets that made prior work tractable.

Closing this gap requires datasets where simplex-position labels are assignable reliably, enabling direct confirmation of whether the model uses belief geometries to track underlying abstract states. Building such datasets is the concrete next step this work motivates.

7.3 Limitations

Effect sizes are modest. The best steering score (0.419) is well below 1.0, and steering null cluster scores overlap with most real clusters, limiting its discrimination. Barycentric R^2 margins are stronger for the clearest clusters (e.g. 512_181: 0.235 vs. 0.160; 512_504: 0.441 vs. 0.307) but modest for others, consistent with simplex structures being present but partially encoded.

Phantom vertices and dissociated signals. As discussed in Section 6.1, V2 of 768_596 has document accuracy 0.069 and its near-vertex examples correspond to a default rather than a semantically crisp state. Phantom vertices are likely a common feature of unsupervised simplex fitting on naturalistic text and may affect other clusters not highlighted here.

No causal proof of belief-state tracking. Our evidence is correlational (barycentric R^2 , KL) or weakly causal (steering). The findings are consistent with belief-like state tracking but do not rule out alternative explanations such as correlated surface features spanning the fitted simplex.

Single model and layer. All real-model results are from Gemma-2-9B, layer 20. Whether findings generalize to other models, architectures, or layers is unknown.

8 Conclusion

We have introduced and validated a pipeline for discovering simplex-structured representational geometries in SAE latent spaces of language models. In a controlled toy model the pipeline recovers known simplex structures. Applied to Gemma-2-9B, the barycentric predictive advantage test discriminates real candidates from null: 5 of 13 priority clusters pass on at least one evaluation split; no null cluster passes on either. Cluster 768_596 is the only case where prediction and causal steering jointly support the simplex geometry.

These findings constitute preliminary evidence that Gemma-2-9B’s SAE latent space contains subspaces encoding genuine mixture representations of functionally distinct latent states. The principal remaining obstacle is the absence of structured, verifiable evaluation datasets for naturalistic discourse variables. Future work should construct such datasets and extend the pipeline to additional layers and model families.

9 Reproducibility

The code is available at <https://github.com/good-epic/finding-belief-geometries>. Submit issues on github or email the author with questions or problems.

The author leveraged LLMs in the following ways to complete this work:

- *Literature review and background research*
- *Learning new concepts*. For example, I was not familiar with optimal transport theory before this project and used both reading and Q&A with LLMs to learn about it.
- *Programming assistance*. I wrote inline with Cursor and leveraged Claude Code to write code from scratch after extensive specification. I reviewed all code to ensure it was correct and functional.
- *Drafting the paper*. I interactively developed an outline and first draft with Claude Code, then extensively edited and revised. I subsequently asked for skeptical rereads as well.

References

- Ekin Akyürek, Dale Schuurmans, Jacob Andreas, Tengyu Ma, and Denny Zhou. What learning algorithm is in-context learning? investigations with linear models. In *International Conference on Learning Representations*, 2023.
- Joseph Bloom, Trenton Bricken, et al. SAELens: Towards scalable open-source sparse autoencoders. GitHub repository, 2024. URL <https://github.com/jbloomAus/SAELens>.
- Trenton Bricken, Adly Templeton, Joshua Batson, Brian Chen, Adam Jermy, Tom Conerly, Nick Turner, Cem Anil, Carson Denison, Amanda Askell, et al. Towards monosemanticity: Decomposing language models with dictionary learning. *Transformer Circuits Thread*, 2023. URL <https://transformer-circuits.pub/2023/monosemanticity/>.
- Hoagy Cunningham, Aidan Ewart, Logan Riggs, Robert Huben, and Lee Sharkey. Sparse autoencoders find highly interpretable features in language models. 2023.
- Adele Cutler and Leo Breiman. Archetypal analysis. *Technometrics*, 36(4):338–347, 1994.
- Anil Damle, Victor Minden, and Lexing Ying. Simple, direct and efficient multi-way spectral clustering. *Information and Inference: A Journal of the IMA*, 8(1):181–203, 2019. doi: 10.1093/imaiai/ia008. Advance access published 27 June 2018.
- Nelson Elhage, Tristan Hume, Catherine Olsson, Nicholas Schiefer, Tom Henighan, Shauna Kravec, Zac Hatfield-Dodds, Robert Lasenby, Dawn Drain, Carol Chen, Roger Grosse, Sam McCandlish, Jared Kaplan, Dario Amodei, Martin Wattenberg, and Christopher Olah. Toy models of superposition. 2022.
- Wes Gurnee and Max Tegmark. Language models represent space and time. In *International Conference on Learning Representations*, 2024.
- Wes Gurnee, Emmanuel Ameisen, Isaac Kauvar, Julius Tarnag, Adam Pearce, Chris Olah, and Joshua Batson. When models manipulate manifolds: The geometry of a counting task. 2026.
- Subhash Kantamneni and Max Tegmark. Language models use trigonometry to do addition. 2025.
- Sarah E. Marzen and James P. Crutchfield. Predictive rate-distortion for infinite-order Markov chains. *Journal of Statistical Physics*, 168(6):1312–1339, 2017.
- Guilherme Penedo, Hynek Kydlíček, Loubna Ben allal, Anton Lozhkov, Margaret Mitchell, Colin Raffel, Leandro Von Werra, and Thomas Wolf. FineWeb: Decanting the web for the finest text data at scale. *arXiv preprint arXiv:2406.17557*, 2024.

Mateusz Piotrowski, Paul M. Riechers, Daniel Filan, and Adam S. Shai. Constrained belief updates explain geometric structures in transformer representations. 2025.

Paul M. Riechers, Thomas J. Elliott, and Adam S. Shai. Neural networks leverage nominally quantum and post-quantum representations. 2025.

Adam S. Shai, Sarah E. Marzen, Lucas Teixeira, Alexander Gietelink Oldenziel, and Paul M. Riechers. Transformers represent belief state geometry in their residual stream. In *Advances in Neural Information Processing Systems*, 2024. arXiv:2405.15943.

David van Dijk, Daniel B. Burkhardt, Matthew Amodio, Alexander Tong, Guy Wolf, and Smita Krishnaswamy. Finding archetypal spaces using neural networks, 2019.

Aarthi Venkat, Scott E. Youlten, Beatriz P. San Juan, Carley Purcell, Matthew Amodio, Daniel B. Burkhardt, Andrew Benz, Jeff Holst, Cerys McCool, Annelie Mollbrink, Joakim Lundeborg, David van Dijk, Leonard D. Goldstein, Sarah Kummerfeld, Smita Krishnaswamy, and Christine L. Chaffer. AAnet resolves a continuum of spatially-localized cell states to unveil tumor complexity. bioRxiv preprint, 2024. doi:10.1101/2024.05.11.593705.

Johannes von Oswald, Eyvind Niklasson, Ettore Randazzo, João Sacramento, Alexander Mordvintsev, Andrey Zhmoginov, and Max Vladymyrov. Transformers learn in-context by gradient descent. In *International Conference on Machine Learning*, 2023.

Dingding Wang, Chris Ding, and Tao Li. K-subspace clustering. In *Machine Learning and Knowledge Discovery in Databases (ECML PKDD 2009)*, volume 5782 of *Lecture Notes in Computer Science*, pp. 506–521. Springer, 2009.

Sang Michael Xie, Aditi Raghunathan, Percy Liang, and Tengyu Ma. An explanation of in-context learning as implicit bayesian inference. In *International Conference on Learning Representations*, 2022.

A Toy Model: Proof of Concept

Generator and Setup

We construct a multipartite (MP) process by independently drawing emissions from five component models: three Mess3 hidden Markov models (Marzen & Crutchfield, 2017) and two Tom Quantum (Bloch Walk) generalized HMMs (Riechers et al., 2025). The three Mess3 instances have parameters $(x, a) \in \{(0.05, 0.85), (0.075, 0.90), (0.10, 0.95)\}$; the two Tom Quantum instances have parameters $(\alpha, \beta) \in \{(1.51, 3.07), (1.99, 2.51)\}$. The joint vocabulary is $4 \times 4 \times 3 \times 3 \times 3 = 432$ tokens.

This setup is *intentionally challenging*. Each token jointly encodes contributions from all five independent sources, creating high conditional entropy: random guessing achieves 0.2% top-1 accuracy, and even a well-trained transformer achieves only modest accuracy. We chose this regime because we expected real-model belief geometries to be partially obscured by noise and entanglement between co-occurring features. A small transformer ($d_{\text{model}} = 128$, 4 heads, 3 layers, context length 16) achieves 7.1% top-1 accuracy, confirming meaningful learning while remaining far from saturation.

Recovery Results

We fit TopK SAEs ($K \in \{3, 4, 5, 6, 7, 8, 10, 12, 14, 16, 19, 22, 25\}$, $d_{\text{SAE}} = 256$) to each layer, apply k -subspace clustering to the decoder matrix, and fit AAnet with target simplex dimensions $K \in \{2, 3, 4, 5\}$, selecting K by elbow criterion. For the Mess3-associated clusters the elbow consistently falls at $K = 3$, correctly identifying the underlying 2-simplex. Table 4 shows results from the best hyperparameter setting (TopK $K = 12$, $N = 6$ clusters, layer 1). All five generative components are recovered by a unique, non-conflicting cluster with a mean R^2 of 0.61 on held-out data. This is a nontrivial result: the residual stream encodes multiple component signals along shared linear directions (cross-component entanglement),

yet the pipeline recovers all five components with no supervision. Per-component PCA projections and representative latent activation patterns illustrating this entanglement and the pipeline’s recovery are shown in Appendix B.

Table 4: **Toy model clustering recovery (R^2), layer 1.** Each cluster is assigned to the generative component whose belief state it best predicts (linear regression, held-out data). All five components are recovered with no conflicts. R^2 values are modest but uniformly positive, consistent with genuine but partial recovery under the high-entropy multipartite setting.

Cluster	Assigned component	R^2
0	tom_quantum	0.551
1	mess3_2	0.314
2	tom_quantum_1	0.577
3	mess3_1	0.719
4	mess3	0.893
5	(noise)	—
Mean (assigned clusters)		0.611

Process Details

Mess3 process. A Mess3 HMM (Marzen & Crutchfield, 2017) has three hidden states $\{0, 1, 2\}$ with transition probabilities parameterized by (x, a) : the self-transition probability is a , and the remaining probability $1 - a$ is split uniformly among the other two states. The emission from state s is token s with probability x and a random token with probability $1 - x$.

Tom Quantum (Bloch Walk) process. The Bloch Walk GHMM (Riechers et al., 2025) is parameterized by (α, β) controlling the step distribution on the Bloch sphere. The internal state is a unit vector on S^2 ; emissions are four tokens corresponding to projective measurements.

Multipartite model vocabulary. The MP model generates tuples from $\{0, \dots, 3\}^2 \times \{0, 1, 2\}^3$, encoded as a single integer token from $\{0, \dots, 431\}$.

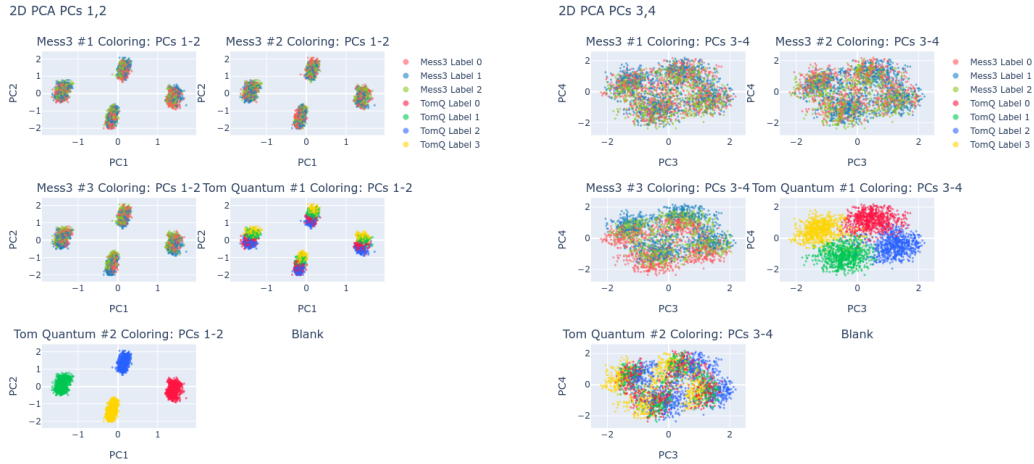
B Toy Model: Per-Component PCA Projections and Latent Patterns

Figure 3 shows the best PCA projections for each of the five generative components at layer 1, colored by ground-truth belief state. Different components are best revealed by different principal components. More strikingly, every panel also exhibits clear token-class separation for at least one other sub-component, demonstrating cross-component entanglement: the residual stream encodes multiple independent generative sources along the same linear directions. The TQ1 projection (PCs 3–4) simultaneously reveals clear separation for TQ2 and M33; the M31 and M32 projections each show near-perfect separation for the other. Despite this entanglement, the recovered clusters achieve a mean R^2 of 0.61 (Table 4).

Figure 4 shows the empirical probability density functions for all latents in the best natural cluster at layer 1 (Cluster 4, $R^2 = 0.89$). Individual latents concentrate in distinct regions of each component’s belief geometry, demonstrating geometry-consistent partitioning of belief-state information across latents.

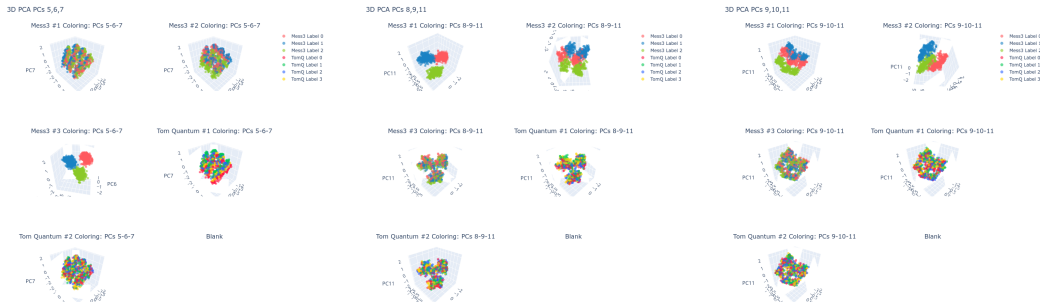
C SAE Details

We use the Gemma-2-9B SAE from the SAELens library (release gemma-scope-9b-pt-res, layer 20, expansion factor ≈ 4.6 , average L0 ≈ 68 active features per token). The SAE was



(a) **Tom Quantum 2, PCs 1–2.** TQ2’s token classes are fully separated; TQ1’s token classes are also clearly separated in this same subspace.

(b) **Tom Quantum 1, PCs 3–4.** TQ1’s token classes separate cleanly; the same subspace also reveals clear separation for TQ2 and M33—three independent sub-components simultaneously legible in a single 2D projection.



(c) **Mess3 #3, PCs 5–6–7.** Triangular (2-simplex) structure for M33; TQ1 and M32 separation also visible.

(d) **Mess3 #1, PCs 8–9–11.** M31’s triangular geometry; M32’s classes are near-perfectly separated in this same subspace.

(e) **Mess3 #2, PCs 9–10–11.** M31’s classes are simultaneously near-perfectly separated.

Figure 3: Per-sub-component PCA projections, toy model layer 1. Each panel shows the PCA subspace that best reveals one sub-component’s geometry, colored by that component’s true discrete output token. Every panel also exhibits clear separation for at least one other sub-component, demonstrating cross-component entanglement.

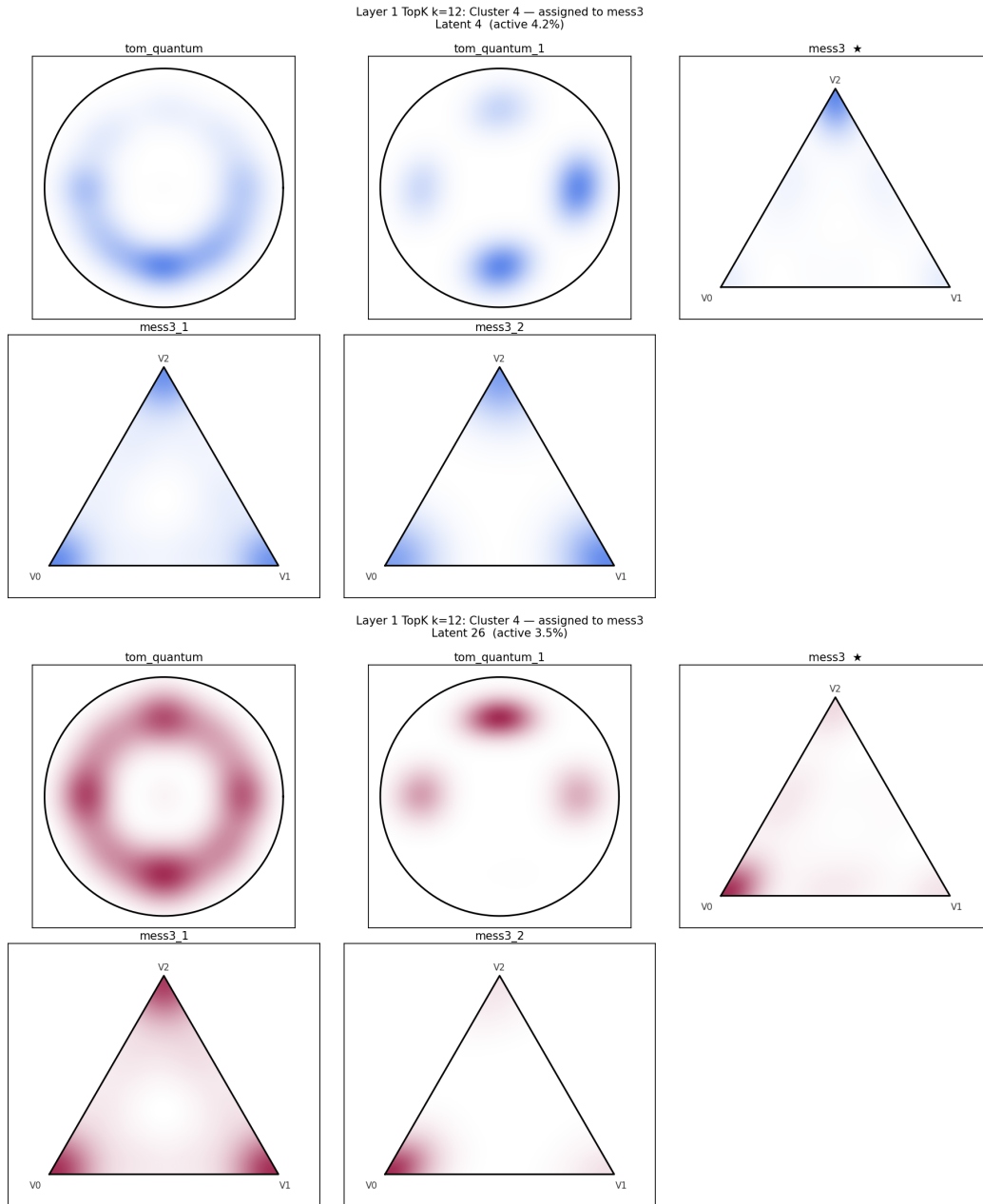


Figure 4: **Two representative latents from Cluster 4 (multipartite toy model, layer 1, TopK $K = 12$).** Each panel shows KDE-smoothed activation density over all five component belief geometries. The assigned component is marked \star ($R^2 = 0.89$). *Top:* Latent 4 fires near the top vertex of each Mess3 simplex and at the centre of the Tom Quantum disks. *Bottom:* Latent 26 fires near the base vertices and along the annular rim of the Tom Quantum disks. The two latents tile complementary regions of the same geometry, demonstrating geometry-consistent partitioning of belief-state information.

trained by DeepMind on a proprietary mixture of text data using JumpReLU activation with L_2 reconstruction loss.

For the toy model SAEs, we use a custom TopK SAE implementation with $d_{\text{SAE}} = 256$, training for 20,000 steps on sequences generated online from the MP model. We tried

$K \in \{3, 4, 5, 6, 7, 8, 10, 12, 14, 16, 19, 22, 25\}$; the best-recovering SAE for the Mess3 component uses $K = 3$.

D AANet Architecture and Training

We use the AANet implementation from van Dijk et al. (2019). The encoder consists of two hidden layers (widths 256, 128 by default), a bottleneck of dimension $K - 1$ (to enforce the simplex constraint via softmax normalization), and an analogous decoder. The loss combines L_2 reconstruction, a simplex penalty $\lambda_1(1 - \|\mathbf{E}(a)\|_1)$, and a non-negativity penalty $\lambda_2 \sum_i |x_i| \mathbf{1}(x_i < 0)$. We train with AdamW, learning rate 10^{-3} , for 10,000 steps, selecting the checkpoint with the lowest validation reconstruction loss, averaged across 5 independent restarts.

E Causal Steering Intervention Types

The three intervention types differ in how long the steering delta is sustained during generation. In all cases the delta is the AANet-derived direction toward the target vertex, added to the residual stream at scale s .

- **Type 1:** Single-position patch. The delta is added only to the cached residual at the trigger position; subsequent generated tokens attend to this modified position via the KV cache but are not directly patched.
- **Type 2:** Sustained window patch. The delta is injected into each newly computed position for the first k_{sustain} generated tokens after the trigger, then generation proceeds freely.
- **Type 3:** Fully sustained patch. The delta is applied to every generated position throughout the full continuation.

F Barycentric vs. Best-Latent R^2 : Detailed Plots

Figures 5–7 show the full R^2 comparison plots for the three clusters with a significant barycentric advantage on near-vertex samples. Each figure contains a box plot comparing per-token R^2 distributions (left) and a paired scatter plot where points above the diagonal indicate tokens where bary wins (right).

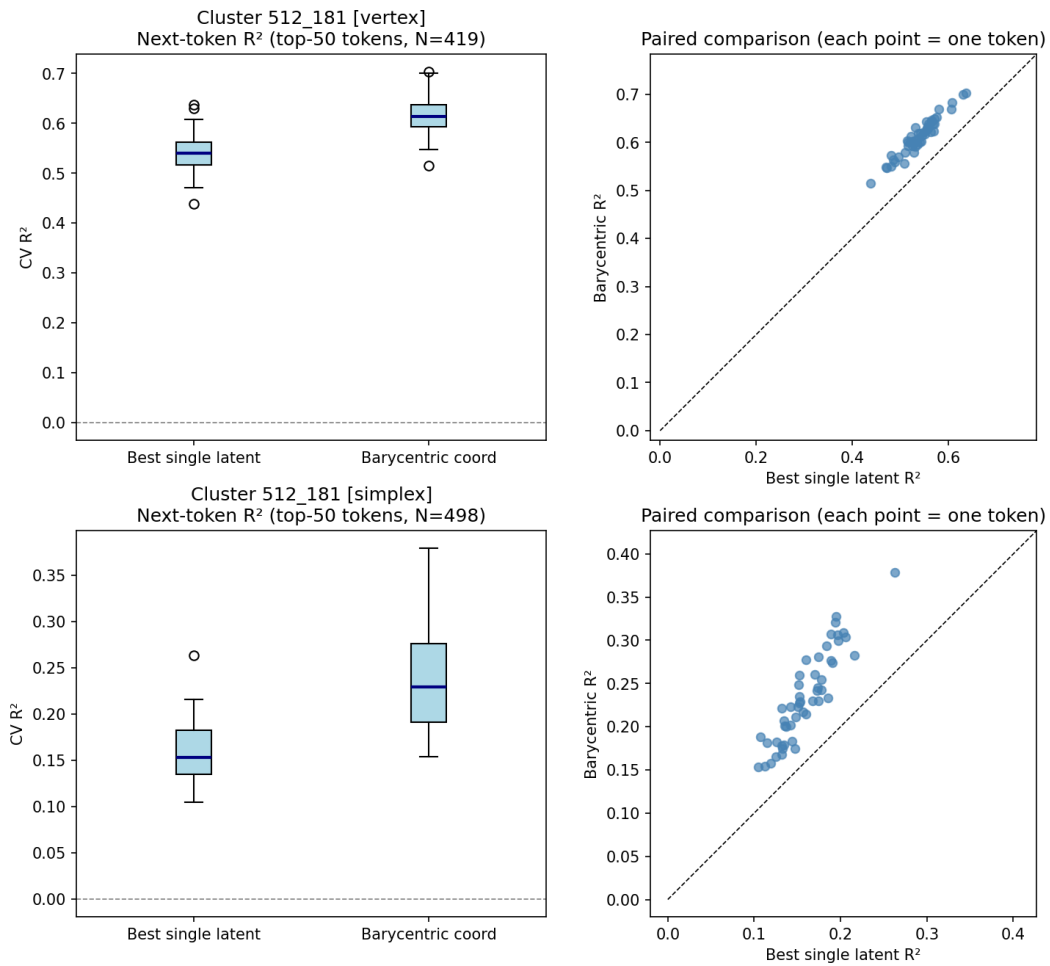


Figure 5: **Cluster 512.181: barycentric vs. best-latent R^2 .** Barycentric coordinates (mean $R^2 = 0.612$) outperform the best individual latent (mean $R^2 = 0.539$) for every one of the 50 tokens (Wilcoxon $p < 10^{-15}$).

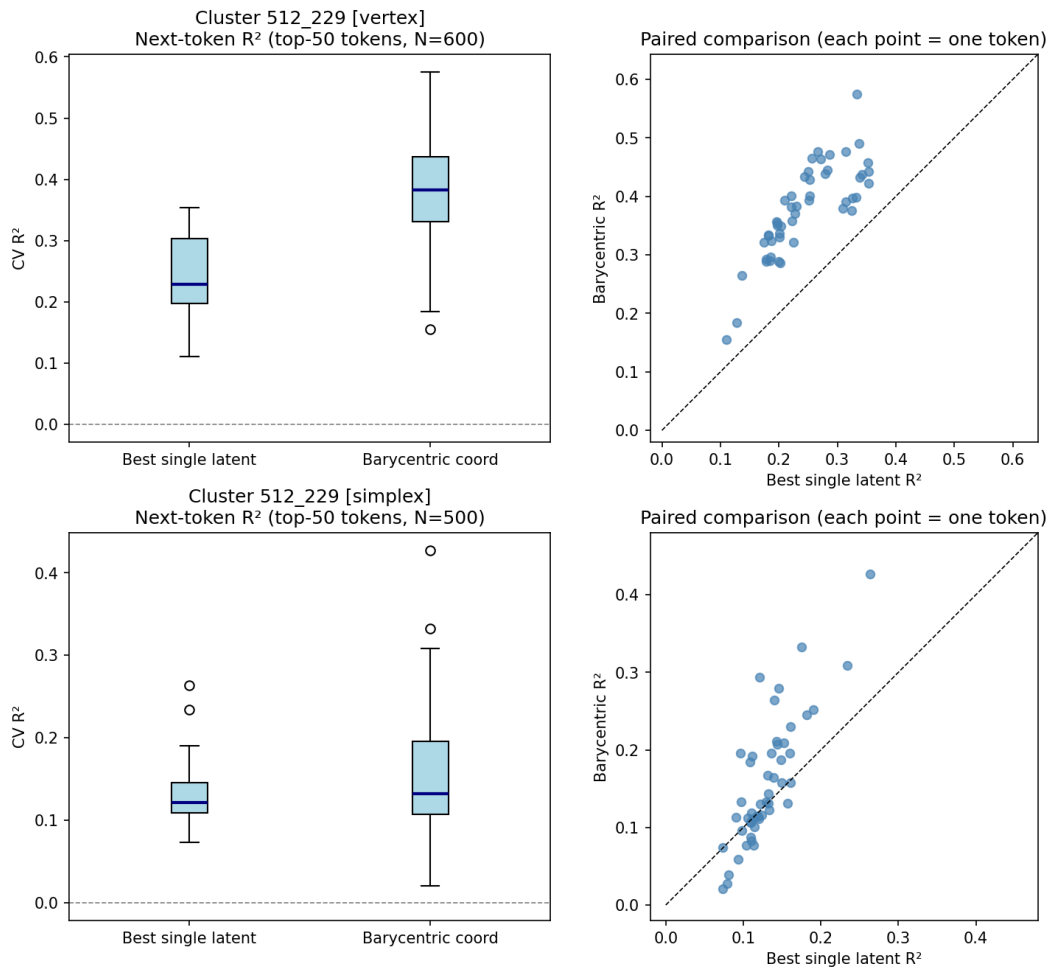


Figure 6: **Cluster 512_229: barycentric vs. best-latent R^2 .** Barycentric coordinates (mean $R^2 = 0.378$) outperform the best individual latent (mean $R^2 = 0.244$) for all 50 tokens (Wilcoxon $p < 10^{-15}$), with a $\sim 55\%$ relative improvement.

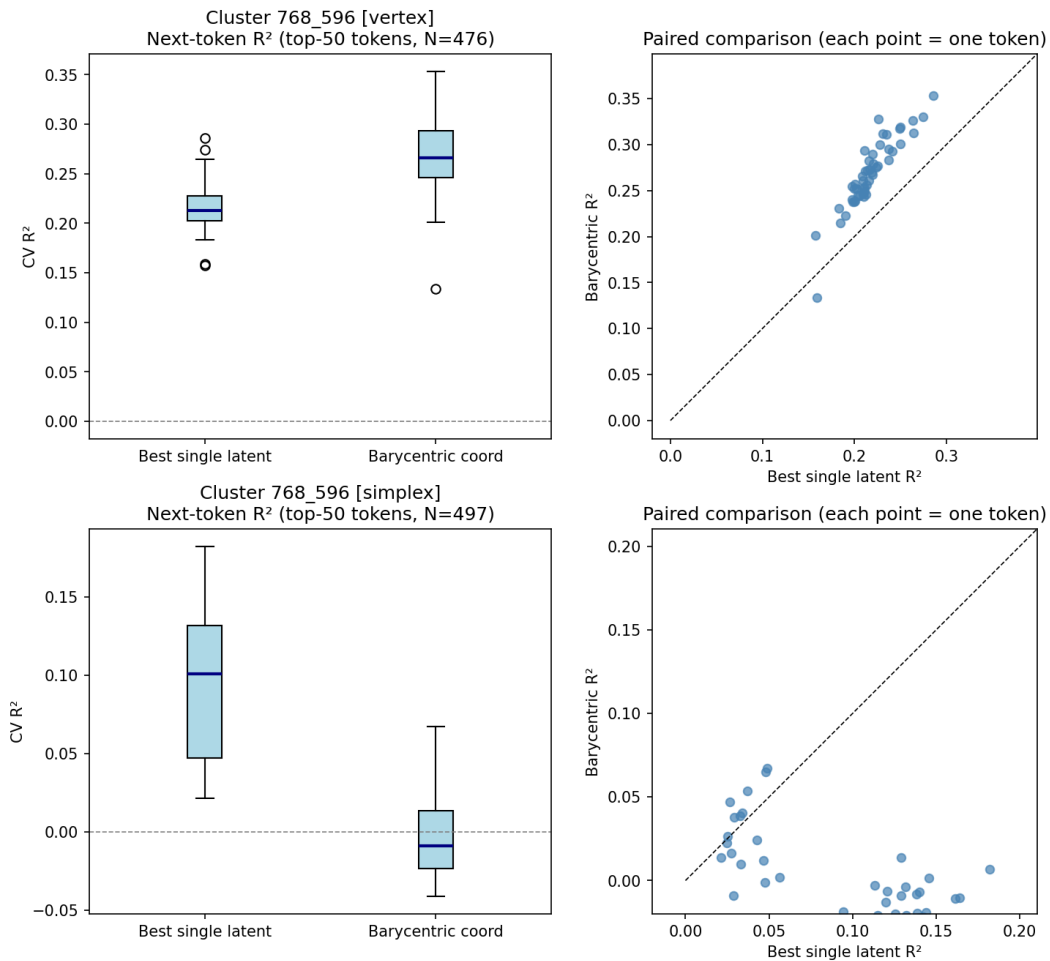


Figure 7: **Cluster 768_596: barycentric vs. best-latent R^2 .** Barycentric coordinates (mean $R^2 = 0.269$) outperform the best individual latent (mean $R^2 = 0.217$) for 98% of tokens (Wilcoxon $p < 10^{-14}$). This cluster also has the highest causal steering score (0.419).

G All Priority Cluster Results

H Per-Cluster Latent Catalogue

For each of the four clusters with the strongest functional evidence—the highlight cluster (768_596), the two clusters with the largest barycentric margins (512_181, 512_229), and the cluster with the strongest KL signal and semantic interpretation (768_140)—we list every cluster latent alongside its Neuronpedia GPT-4o-mini auto-interpretation and the simplex vertex(es) at which it is active in near-vertex samples.

A latent is counted as *active at vertex v* if its mean activation across near-vertex- v samples accounts for at least 1% of the total mean activation summed across all cluster latents at that vertex. The **pie%** column reports this fractional share; a dash (—) indicates the latent did not reach the 1% threshold at any vertex.

Table 5: **Full results across all four validation strands.** KL ratio: cross/same symmetric KL divergence ratio. Bary wins: fraction of top-50 tokens where $R^2_{\text{bary}} > R^2_{\text{best latent}}$ (“sig.” if Wilcoxon $p < 0.001$). Steering: best-combination score (“—” if cluster did not qualify). Interp.: frontier-LLM vertex label consistency (HIGH/MED/LOW).

Cluster	m	KL ratio	Bary wins	Steering	Interp.
512_17	15	1.054	0.00	0.118	HIGH
512_22	6	1.058	0.00	0.356	LOW
512_67	25	1.229	0.00	0.250	LOW
512_181	26	1.037	1.00 (sig.)	—	LOW
512_229	22	1.166	1.00 (sig.)	—	MED
512_261	18	1.032	0.00	0.242	MED
512_471	10	1.017	0.00 [†]	—	LOW
512_504	22	1.164	0.00 [†]	—	MED
768_140	26	1.987	0.20	0.289	MED
768_210	4	1.017	0.00	0.336	MED
768_306	5	1.102	0.16	—	MED
768_581	11	1.144	0.00	0.209	LOW
768_596	6	1.037	0.98 (sig.)	0.419	MED
512_138 (null)	51	1.329	0.00	0.358	—
512_345 (null)	47	1.311	0.02	0.150	—
768_310 (null)	17	1.108	0.16	0.272	—

[†] Bary wins 0% on near-vertex samples but significant on simplex-interior samples (512_471: 84%, 512_504: 100%, both $p \approx 0$).

Cluster 512_181 $k = 3$, **synthesis confidence: low**

- V0** (mixed): Content words and lexical items carrying semantic meaning.
- V1** (mixed): Function words and determiners serving grammatical roles.
- V2** (inconsistent): Technical/specialized terminology OR prepositions and connectives.

Latent	Neuronpedia interp (GPT-4o-mini)	Active at (pie%)
L2149	Occurrences of research methodologies and results in scientific texts	V1 (19%)
L2318	Instances of error logging and debugging messages in code	—
L2759	Programming constructs and function calls associated with database management	—
L3510	Mathematical expressions related to derivatives	—
L3954	Mathematical concepts related to derivatives and calculus	—
L4321	References to privilege and inequality in social contexts	V1 (73%)
L4389	References to legal principles and judicial interpretations	—
L4741	References to educational contexts and programming structures	—
L6538	Genetic and phenotypic differences between mutant and wild-type organisms	—
L7419	Terms related to specialized or technical concepts in various fields of study	—
L7988	Structured data, possibly focusing on code or programming attributes	—

Latent	Neuronpedia interp (GPT-4o-mini)	Active at (pie%)
L8095	API request parameters and their associated values	—
L8509	Technical terms and references related to programming and system processes	—
L9055	Elements related to variable names and their associated values within programming code	—
L10207	Structured elements and data types in programming code	V2 (49%)
L11115	Data values and statistical metrics related to medical research	—
L11611	Metrics and effects related to dietary treatments in clinical or experimental contexts	V1 (2%)
L12475	Structured programming syntax elements and errors	V2 (3%)
L14402	Programming or coding-related syntax and structures	—
L15310	Elements related to mathematical operations or functions in coding	—
L15334	Elements related to data structures and their connections	V0 (97%), V2 (48%)
L15367	References to specific legal and regulatory terms	V1 (3%)
L15676	Components and notations related to mathematical and physical formulas	—
L15798	Technical terms and structures related to electrical engineering and data processing	—
L16183	Specific mentions of maps and locations	—
L16184	Mentions of numerical values or mathematical parameters	—

Cluster 768_140 $k = 3$, synthesis confidence: medium

V0 (mixed): Generic/indefinite reference (common nouns, articles, abstract concepts).

V1 (consistent): Specific/definite reference (proper nouns, named entities, dates, locations).

V2 (mixed): Contextual/anaphoric reference (pronouns, demonstratives, function words).

Latent	Neuronpedia interp (GPT-4o-mini)	Active at (pie%)
L449	Special characters, particularly underscores and certain punctuation marks	—
L1234	Various forms of punctuation and mathematical symbols	—
L1367	References to academic papers and their citation formats	—
L1462	Quotes or dialogue from characters or people	V0 (5%)
L1575	References to experimental findings and numerical data	—
L1993	Punctuations and metadata references within the text	—
L2493	Quotes, citations, and references from authoritative figures or texts	—
L2756	Punctuation and formatting signals in the text	V0 (3%)
L2878	Emotional expressions and sentiments related to personal connections	V1 (2%)

Latent	Neuronpedia interp (GPT-4o-mini)	Active at (pie%)
L3771	Direct quotations and dialogue in the text	V0 (7%)
L3988	Instances of dialogue and quotation marks	—
L4449	Quotations and speech indicators	V0 (3%)
L4927	Phrases that signal emphasis or specificity in statements	—
L5030	Elements related to JavaScript code and function definitions	—
L6432	Elements related to storytelling and narrative structure	—
L7176	Quoted speech and dialogue within the text	V0 (26%)
L8015	Terms related to online services and technology	V2 (1%)
L8868	Critical events and significant moments in various contexts	V1 (13%)
L9395	Dialogue and quotes from individuals within the text	V0 (6%)
L10473	Scientific terms related to medical and biological research contexts	—
L10536	References to specific warranty policies and legal terms	V0 (40%)
L11869	Quotes and references to statements made by individuals in a critical context	V0 (1%), V1 (2%)
L12387	Phrases that indicate personal reflection or apology	V0 (2%)
L13511	Keywords related to medical research and development	V2 (97%)
L15111	Instances of emphasis or quotes around significant concepts	V0 (8%)
L16340	Informational or procedural text related to finance and taxes	V1 (82%)

Cluster 768.596 $k = 3$, synthesis confidence: medium

V0 (mixed): Third-person references and impersonal/descriptive constructions.

V1 (mixed): First-person perspective and subjective expression.

V2 (mixed): Second-person address and directive/instructional language.

Latent	Neuronpedia interp (GPT-4o-mini)	Active at (pie%)
L4269	Code-related syntax and structures	—
L7398	Conversational expressions and phrases	V1 (2%), V2 (100%)
L9729	Punctuation marks and their contexts within sentences	—
L12076	Questions related to religious practices and their origins	V1 (2%)
L13939	References to non-profit organizations and charitable donations	V1 (97%)
L14895	Code-related terms and programming concepts	V0 (99%)

Cluster 512.229 $k = 3$, synthesis confidence: medium

V0 (consistent): Simple syntactic structures: isolated words, basic phrases, common function words.

V1 (mixed): Formal/technical content: proper nouns, dates, specialized terminology.
V2 (consistent): Complex syntactic structures: dense modification, embedded clauses.

Latent	Neuronpedia interp (GPT-4o-mini)	Active at (pie%)
L1189	Snippets of mathematical or programming expressions and logical statements	—
L1277	References to individuals in positions of authority or influence	—
L1425	References to historical events and their impacts on society	—
L1481	References to educational institutions and their operational details	V1 (16%)
L1540	Words indicative of financial or economic conditions and events	V1 (2%)
L1818	Punctuation and markup elements in text	—
L3373	Specific dates and numbers, particularly related to events or data points	V1 (15%)
L5990	References to specific scientific publications and data repositories	—
L6370	Specific numerical data and dates associated with events	V1 (7%)
L7478	References to specific locations, organizational names, and demographic details	V1 (1%)
L7833	Numerical and procedural references in formal documents and academic contexts	V0 (100%), V2 (100%)
L8269	Occurrences of specific dates and times	V1 (11%)
L8501	Keywords related to financial burdens and energy-related issues	—
L8625	Time-related terms and dates	V1 (5%)
L9122	Statements related to programming constructs and their syntax	V1 (1%)
L9805	Economic indicators related to inflation and consumer behavior	V1 (2%)
L13248	Patterns in structured data or code, relating to token identifiers or variables	—
L13972	Details related to historical events and patent information	—
L14155	Numbers and financial figures related to statistics	V1 (31%)
L14760	Specific dates and numerical data	V1 (2%)
L15855	Numerical values and specific identifiers related to data points	V1 (5%)
L16151	Indicators of conditional statements and significance	—